

NONLINEAR BEAM DYNAMICS IN A FUNNEL FOR COMBINING TWO INTENSE ION BEAMS*

J.H. Whealton, R.J. Raridon, K.E. Rothe,
W. R. Becraft,[†] and T.L. Owens,[‡]

Oak Ridge National Laboratory, P.O. Box 2009, Oak Ridge, Tennessee 37831-8071 USA

1. Abstract and Introduction

The concept of funnels was introduced over the last few years with an endeavor to increase the beam intensity by combining two beams in the following fashion:

The beam is, in each case, produced by an rf accelerator and thereby composed of bunches. The beam bunches are made to occupy relatively small fractions of the longitudinal phase in these cases. The bunches from each of the two beams are made to interlace and enter an rf deflector which produces the interlacing of the beams into one beam with twice as many bunches occupying twice the phase. The funnel itself, in one embodiment called the magnetic funnel, is composed of many transport elements with strong transverse focusing produced by quadrupole permanent magnetic fields. An occasional rf rebuncher is introduced to recompress the beam longitudinally so the beam occupies the appropriate small fraction of velocity space in the parallel direction. Crucial elements of the funnel are the beam dynamics in the rf rebuncher and in the deflector. Beam dynamics in either case must be assessed using an analysis which we are going to describe below.

Several components in a magnetic¹ funnel have been examined by dint of a full three-dimensional solution to the time-dependent Vlasov-Poisson equations with all image charges included.² Specifically, the rms emittance growth of subsystems is examined in detail. For the systems considered, a significant parallel emittance growth occurs. Details of the cause and ephemerality of this emittance growth are studied. These systems¹ were originally designed using the 2-1/2-D PARMILA-type analysis³ which does not account for image charges and neglects azimuthal nonlinear space charge forces. Designs based on PARMILA are referenced for the subject evaluation. A highly resolved, accurate assessment of rms emittance growth has not been obtained with such analysis. However, for the subject analysis at least the precision is significant as will be shown. First, we will consider the simple rebuncher; second, the rf deflector; and third, we will introduce a nonlinear longitudinal emittance reducing "optical" element. The rms parallel emittance growth is due to the longitudinal velocity kick being

dependent on a transverse dimension as well as the longitudinal dimension forming an oblique surface of zero volume, for example, in the three-dimensional phase; $z, V_z,$ and x . A plane surface parallel to x in this space has zero rms emittance. A curved surface or a plane not parallel to x in this space has finite rms emittance under the conventional definition:

$$\epsilon_{z,rms} = \frac{\beta\gamma}{n} \left\{ \sum_j (z_j^2) \sum_j (z_j'^2) - \left(\sum_j (z_j^2 z_j') \right)^2 \right\}^{1/2}$$

This is considered conventional, because of the protocol suggested by Los Alamos National Laboratory (LANL), and practical, because the occupation in phase space of an uncontrolled surface, even for a moment, eventually makes that surface uncontrollable. To effect control would require two identical particles seeing a different force even when they are in the same position at the same time. Control

must be exerted as soon as possible upon the deviant. Having the longitudinal velocity depend differently on both transverse positions does not help matters as this is what happens in an rf deflector as presently considered.

2. Nonlinear Beam Dynamics in a RF Rebuncher (2-D)

The dynamic systems which we will consider are:

$$\nabla^2 \phi(x,t) = \int f_-(v_-, x, t) dv_- - \exp[-\phi(x,t)/T_e] \quad (1)$$

$$\frac{\partial f_-(v_-, x, t)}{\partial t} + (v_- \bullet \nabla_x) f_-(v_-, x, t) + [\nabla \phi(x,t) \bullet \nabla_{v_-}] f_-(v_-, x, t) = f_0(v_-, x, t) \quad (2)$$

The subject analysis can best be understood with reference to Figure 1, which shows the path of the calculation. First, the Poisson equation is considered. For this first pass, the source terms are set equal to zero and a Laplace equation is solved by SOR, finite difference, and boundary interpolation within a cell, using a Gauss-Seidel implicit method.⁴ Considering the attributes A1, resource utilization, and A2, accuracy, iteration reduces memory requirements (A1), and boundary interpolation contributes to the accuracy per cell (A2). Generally, individual convergence of the solutions is not warranted on each pass (contributes to A1), since the iteration procedure lends itself to incomplete convergence of the intermediate solutions. As noted before, the finite difference method compared with the finite element method has in our experience reduced A1 by a factor of 20 for the Poisson solution (Reference 5 vs Reference 6) for the same accuracy. Boundary conditions for arbitrarily shaped metal surfaces can be specified as time-dependent Dirichlet or ramped Dirichlet conditions (contributes to A2). Neumann boundary conditions can also be specified.

TIME DEPENDENT ALGORITHM

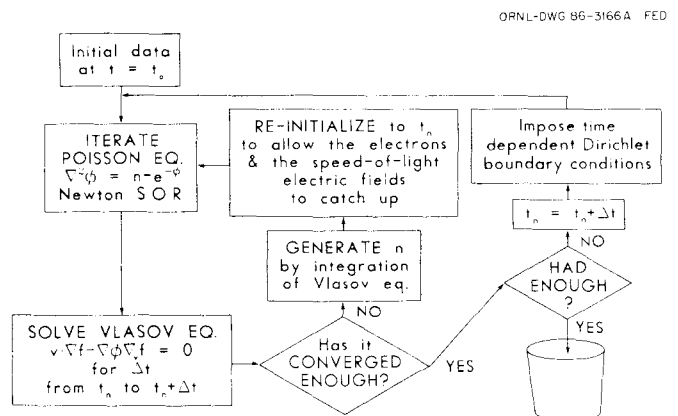


Fig. 1. Path of calculation for 3-D, time-dependent Vlasov-Poisson analysis.

*Research sponsored by the Office of Fusion Energy, U.S. Department of Energy, under contract DE-AC05-84OR21400 with Martin Marietta Energy Systems, Inc.

[†]Consultant, Grumman Space Systems, P.O. Box 3056, Oak Ridge, TN 37831.

[‡]Now at Fermilab

Second, the Vlasov equation is solved for an arbitrary initial condition using the solution to the Laplace equation above for a time step Δt . The technique is described in References 7 and 6 where significant advances in A1 and A2 are reported. Reference 7 speeds up the Vlasov solver by a factor of 10 (contributes to A1) from that in References 8 or 9 while at the same time improving the accuracy by over a factor of 10 (contributes to A2). Reference 6 decreases resource utilization (A1) over Reference 5 by a factor of 400 with the same accuracy. The trivial relationship between the coordinates inside an element and the global elements for the uniform Cartesian grid used in this algorithm allows a factor of 20 (of the 400) savings in the Vlasov solver (A1) over that employed in the irregular elements of Reference 5. As mentioned in Reference 7, the Vlasov solver is made self-regulating in accuracy; trajectory refinement is undertaken only in those places that need it (A2).

Third, charge deposition is done in three dimensions by interpolation over the grid and is "exact" in the sense that as the three-dimensional grid is made more fine and the number of trajectories is increased, a result as accurate as desired can be obtained (A2). Notice that nowhere is any paraxial-like assumption made, and the fields "to all orders" are directly calculated (attribute A3, nonlinear effects). Therefore, aberrations (to all orders) are also directly computed. Other nonlinear optics effects (A3) computed include space charge "to all orders" caused by nonuniform beam density and/or boundaries. (Boundaries cause nonlinear space charge forces also because they alter the delicate dependence of ϕ on r required to keep it linear.)

Fourth, the beam charge and the exponential plasma term (A3) are taken as inhomogeneous terms to the Laplace equation solved in step 1 above. Now the two inhomogeneous terms are, in many cases, large, of opposite sign, extremely nonlinear, and three dimensional. This is the cause of numerical difficulties that were first surmounted (in two-dimensional steady state) in Reference 8. The technique used, accelerated under-relaxation, improved the prior art¹⁰ by a factor of 1000 (A1) in the beam perveance of interest and by a greater factor for higher perveance. Another factor of 10 (A1) increase in speed was achieved, while at the same time the accuracy was increased by more than a factor of 100 (A2) in Reference 9. This technique was extended to three dimensions in References 5 and 6. Essentially the best technique we have found is to use an unconverged Newton SOR outside its established range of validity.¹¹

Fifth, the time is moved back by Δt , the ions are moved back to their phase space positions a time Δt ago, and the Vlasov equation is resolved with the new fields computed from the Poisson equation solution of step 4. The trajectories are different from those computed in step 2 because of the presence of the space-charge terms (steps 3 and 4).

Sixth, since the trajectories of steps 3, 4, and 5 are different from those of step 2, steps 3, 4, and 5 are repeated (Vlasov-Poisson iteration) until no change obtains. This completes the convergence procedure (A2), and it is time to proceed to the next time step. However, one should note the implication of the iteration consisting of steps 5 and 6.

Seventh, the time is advanced by Δt and steps 2 through 6 are repeated. This performs the beam evolution through the device under consideration.

The attributes A1 through A3 provide orbit accuracies of up to 10^{-8} radians in speedy calculations with significant nonlinearities. Six items contributing to a decrease in resource utilization (A1) total about 2×10^9 in the product of memory saved and CPU time (however, the accounting procedure leading to this figure is somewhat ambiguous). Five items contributing to increased accuracy (A2) make an improvement of about 10^6 for a significantly nonlinear problem.

We turn now to a preliminary examination of a 425 MHz rebuncher. A rebuncher is generally a cylindrically symmetric affair as illustrated in Fig. 2. An emittanceless beam bunch of constant density (waterbag) is shown entering the fringe fields of an rf rebuncher. The fields are near the maximum and the nonlinear forces are evident in the accompanying phase space occupation diagrams.

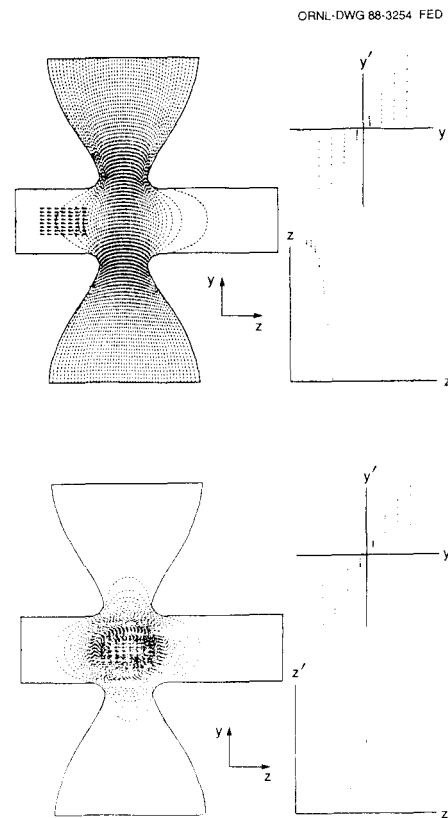


Fig. 2. Rebuncher at two different times.

When the center of the bunch is in the center of the rebuncher, the rf fields are at a null and only the space charge and image charge fields are present. At the end of the rebuncher, the longitudinal phase space occupation is supposed to have a negative slope. Nonlinear shear aberrations are also shown. Longitudinal emittance as a function of time is shown in Fig. 3 for both zero and 100 mA beam current. The double lumped structure represents partial canceling of aberrational shear forces on both sides of the null field (denoted as $\phi=0$ on Fig. 3). The partial cancellation occurs because of the extreme fringe fields such as shown in Fig. 2(a). The radial center of the bunch is molested much more than the edges. As the bunch proceeds, the edge catches up, partially mitigating the aberrations. Immediately after the null, the edge gets more action than the center (overshoots) and the emittance climbs again. Near the trailing edge of the fringe fields, the center catches up again. The net result, at least in the case of zero beam current is that most of the aberrations cancel (90 percent). The reason the rms emittance, at zero current, does not completely round out is that some ion relative motion occurs during traversal of the rebuncher. However, in the high current case in Fig. 3, there is a noticeable space charge/image charge component which is superimposed on the above described shear aberrational phenomena.

The effect of waterbag bunch shape on longitudinal emittance is shown in Fig. 4 (for a somewhat different beam radius). The emittance growth for the hard (square) beam (S0) is significantly greater than the softer (elliptical) beams (S1 and S2); however, there is not much difference between S1 and S2 over the region considered. Numerical noise is 11 orders of magnitude lower than emittance values of interest.

A parallel normalized rms emittance growth on the order of 0.003 ncm. mm. is expected on the "simple" rebuncher. This is in contrast to the negligible growth predicted by PARMILA. Since there are several rebunchers, the total emittance growth due to rebunchers is expected to be higher than 0.003. The complex double rebunchers, necessary near

the rf deflector, will probably add more than this because of the possible degradation of mode purity; the smoothness of the phase space distribution will possibly half this. For the whole funnel the estimated total parallel emittance growth due to the rebunchers is greater than 0.005.

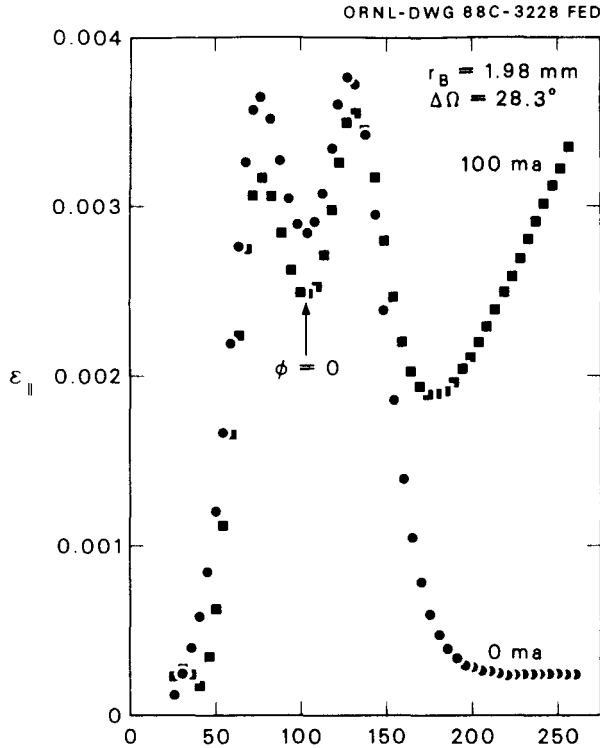


Fig. 3. Longitudinal emittance as a function of time.

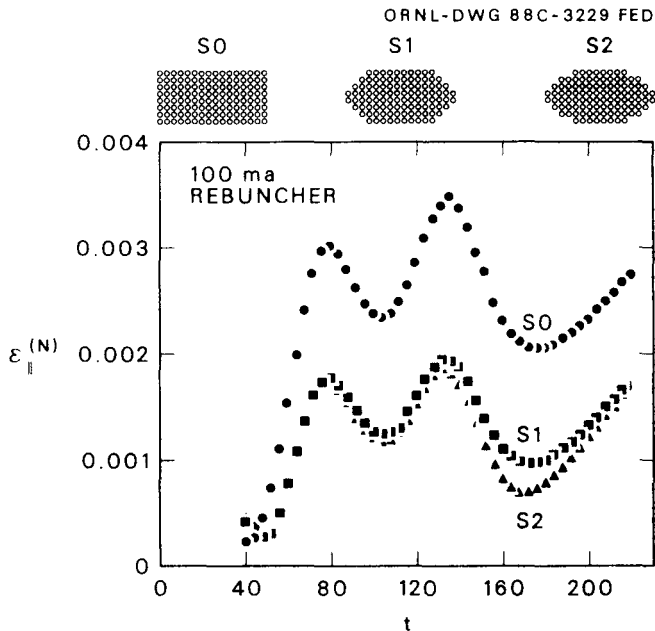


Fig. 4. Effect of beam shape on longitudinal emittance.

3. Nonlinear Beam Dynamics in an RF Deflector (2-D)

Visualization of emittance growth in the rf deflector is aided by reference to a three-dimensional isometric which is shown in Fig. 5. For openers, we are going to consider a two-dimension variant of the deflector by considering strictly slot geometry. This produces some errors which will be checked later.

ORNL-DWG 88-3196 FED

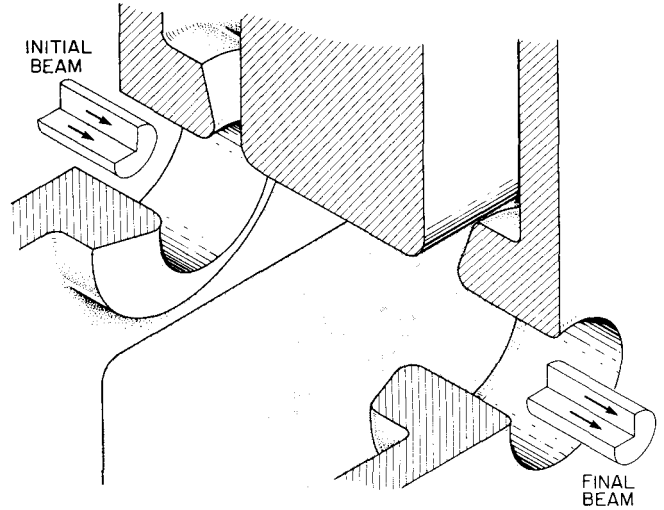


Fig. 5. Isometric of an rf deflector.

Three bunches in an rf deflector are shown at a particular instant of time in the lower part of Fig. 6, labeled B1, B2 and B3. The dashed lines are electric potentials at that instant of time. For this figure, the beam space charge is zero. The potential contours are at linear increments: a coarse increment for extreme potentials, and a finer linear increment near the center of the potential range where the beam bunch is located. Also shown in Fig. 6 are the transverse phase space occupation (upper left-hand side) and longitudinal phase space occupation (middle upper side and expanded on right-hand upper side).

Fringe fields due to the boundary conditions are clearly shown in Fig. 6. The part of the beam bunch nearest the deflector gets kicks in both the transverse and longitudinal directions. The bunches begin with zero emittance. Bunch

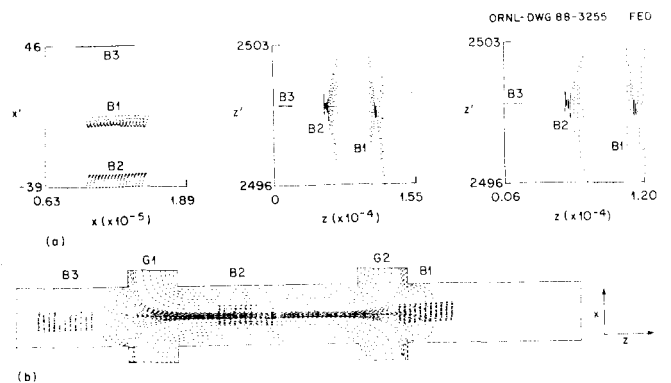


Fig. 6. Phase space occupation and deflector.

number 1, as indicated on the $x-x'$ phase space diagram, is steered approximately into place (aberrations are noticeable); bunch number 2 is approximately 1/3 steered into place also with much aberrations; bunch number 3 shows very little change at this time (as indicated on both the phase space occupation diagrams shown). Longitudinal emittance of bunch number 2 is relatively large as indicated by the B2 $z-z'$ phase diagram while the first bunch parallel emittance is decreasing since the aberrational shear fields in the second gap, G2, are canceling out some of the rms emittance produced by the shear fields in the first gap, G1. At a later time, as illustrated in Fig. 8 taken near a null in the rf driving frequency, bunch number 1 has completed its emittance reduction and B3 is at a maximum in emittance because almost no cancellation has taken place. For 50 mA average beam current, the corresponding cases are shown in Figs. 8 and 9, respectively. Space charge fields interact with the fringe fields in the case of bunch numbers 1 and 3, respectively, in Fig. 8, whereas the main steering force is bent visibly for bunch number 2. The longitudinal emittance is even qualitatively different. The null field illustrated in Fig. 7 for zero current is now dominated by interacting bunches in Fig. 9.

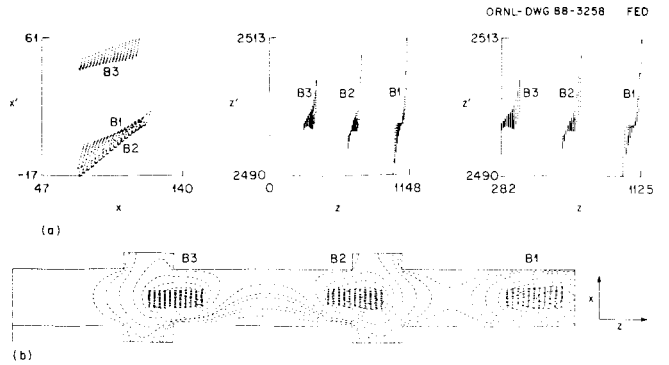


Fig. 9. Phase space occupation and deflector near a null for $I_B = 50$ ma.

Now we will consider the effect of a 425 MHz deflector on a 50 mA beam composed of bunches occupying 28 degrees out of 360 degrees longitudinal phase and 2.5 mm transverse width (see Fig. 10). The longitudinal emittance growth of this bunch is shown in Fig. 11. Both 50 mA and 0 mA are shown in Fig. 11. To get an idea of the properties of such a deflector, we consider first the time reversed deflector in slot geometry. This is done to expedite the calculation. Time reversal is not seriously inhibiting. Similar results apply either way when correctly interpreted. Slot geometry probably shows the emittance growth to within a factor of

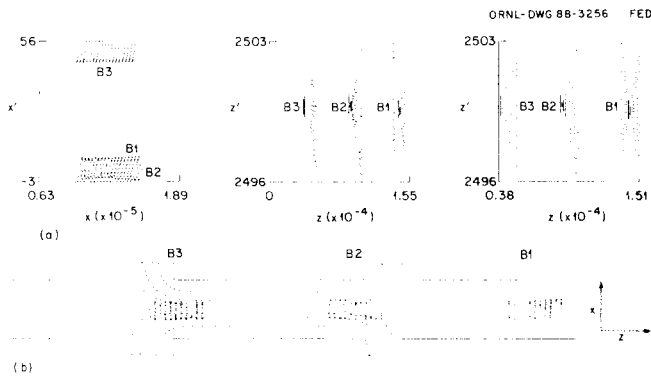


Fig. 7. Phase space occupation and deflector near a null.

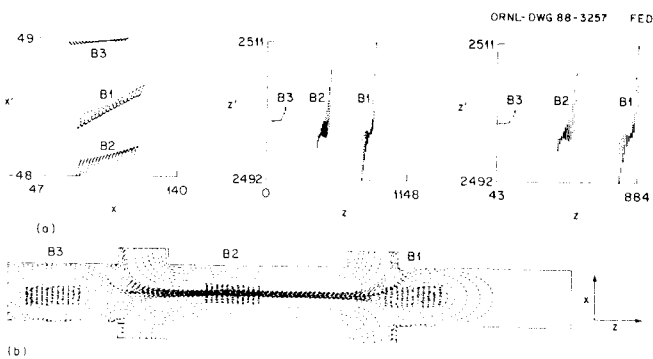


Fig. 8. Phase space occupation and deflector for $I_B = 50$ ma.

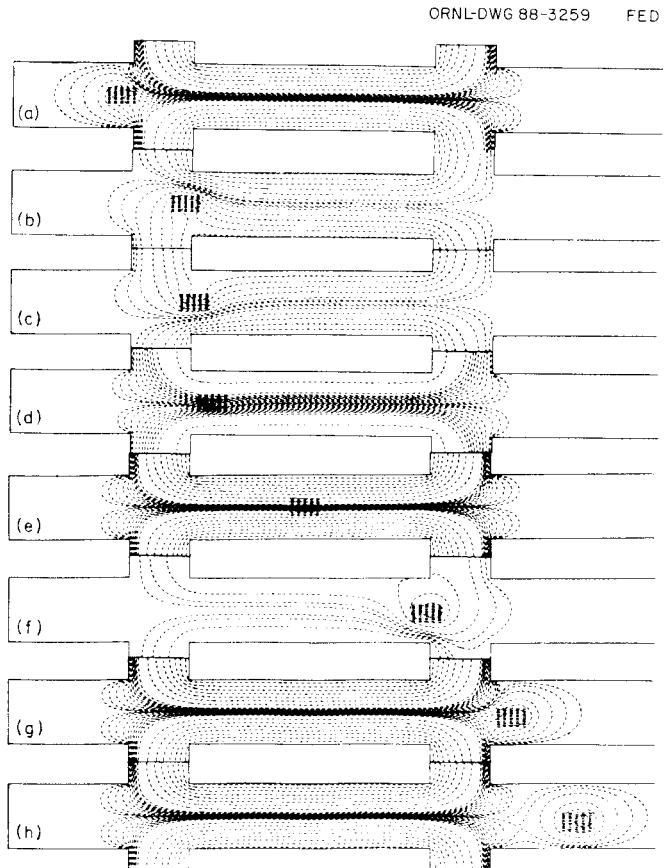


Fig. 10. Bunches occupying 28 degrees out of 360 degrees longitudinal emittance.

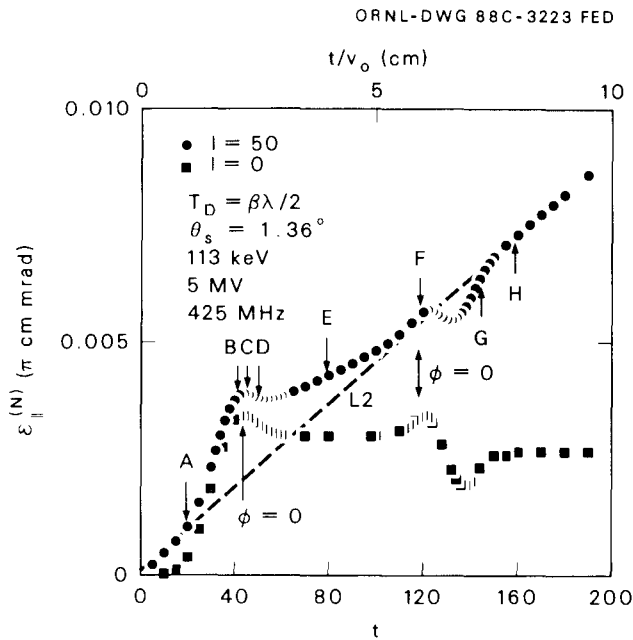


Fig. 11. Longitudinal emittance growth of bunches in Figure 10.

two in either the parallel or transverse direction. An azimuthal nonlinear space charge issue is neglected by such a representation. The main point of the computation is to get a clear idea of the space charge, image charge and applied field aberration issues as quickly as possible, so we can focus on the relevant causes.

In Fig. 10(a), a bunch is entering (leaving) the fringe fields of the deflector. The space charge fields and image charge fields are clearly interacting with the fringe fields. In Fig. 10(b) and 10(c), the time is near an rf null [as is Fig. 10(f)] and the space charge fields dominate the applied rf fields. In Fig. 10(d)-(e), the applied fields dominate, but are clearly perturbed by the space charge fields.

The shear fields are partially canceled by having the field reversed in the gap. This is one of the advantages of having the field reversed in the gap. Another advantage is that the nonlinear shear fields will on the average be smaller in the gap since the rf fields are nearer zero. A major disadvantage is that the steering is mitigated as a result (see Fig. 12 for $T_D = \beta\lambda/2$). As the bunch enters the gap, the steering is initially in the wrong direction; exiting the second gap also produces wrong direction steering. Therefore, the intended steering has to compensate for this. The steering will be less than intended. In this instance, where the thickness of the deflector is $\beta\lambda/2$, the actual steering is 1.36 degrees instead of the 1.50 degrees as planned. Incidentally, the computations agree exactly with the simple calculations (it was only tested to one part in 1000) for the steering in a configuration with no fringe fields. Such a deficit in steering may appear at first sight to be an issue; however, to produce higher steering, say 10 percent higher, requires higher fields in the deflection section which impact reliability and higher heat loading since the rf power to the device is proportional to E^2 , so the rf power/heat loading must go up to 20 percent. There may be a heat dissipation problem even without this inconvenience.

The effect of changing the deflector thickness on the longitudinal emittance growth and steering angle are shown for four values of L: $\beta\lambda/2$, $1.2 \beta\lambda/2$, $0.7 \beta\lambda/2$, and $0.8 \beta\lambda/2$. Emittance growth is shown in Fig. 13 and steering is shown in Fig. 12. A thickness somewhat smaller than $\beta\lambda/2$ appears desirable since the steering increases a few percent with no reverse fringes to counter and the emittance decreases.

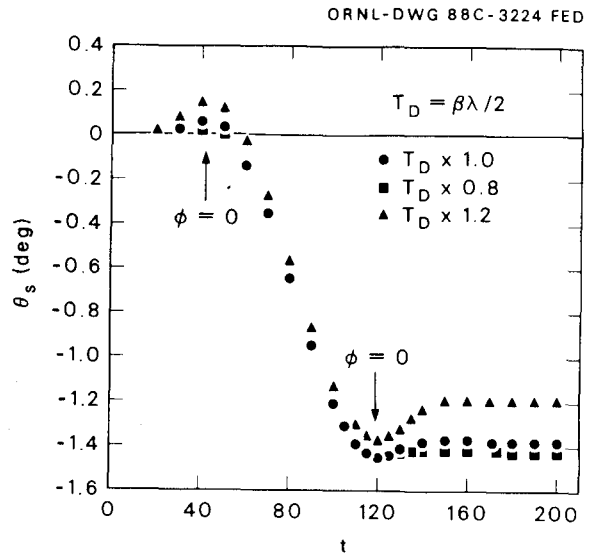


Fig. 12. Rf deflector steering showing mitigation by fringe fields.

Also shown in Fig. 13, is the situation without deflector fields (therefore no field aberrations). The parallel emittance grows, even in this case, about the same as for the thin plate $T_D \sim 0.7 \beta\lambda/2$ case, indicating that virtually all of this emittance growth is due to nonlinear space charge and image charges.

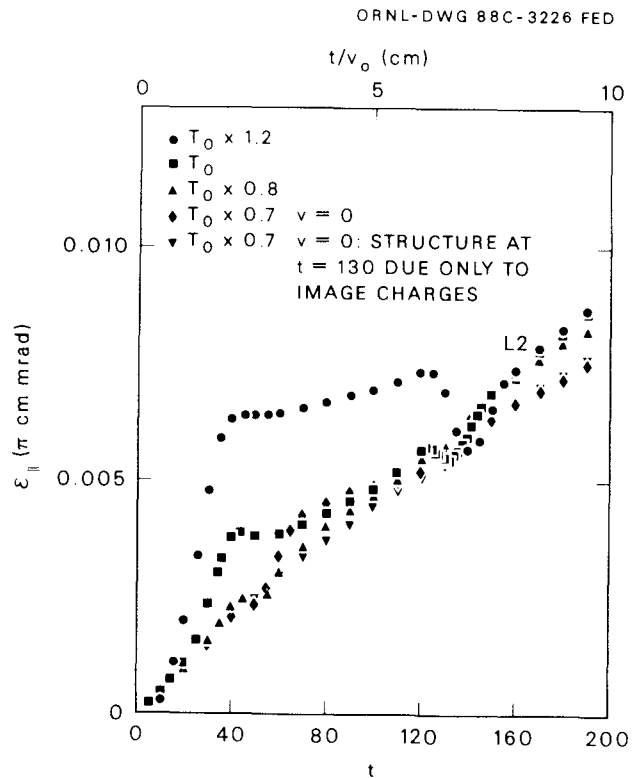


Fig. 13. Effect of deflector thickness on longitudinal emittance growth.

An important feature of Fig. 11 is a qualitative difference between the emittance growth in the high current case and the low current case. The low current case, when not molested by fringe fields, shows no rms emittance growth. However, the high current case seems to suggest a prevailing emittance growth with time, or distance traversed, on which the shear aberrational fields are only a perturbation. This prevailing emittance growth is caused by nonlinear space charge forces and nonlinear image charge forces and is denoted by the line L2.

Results for a 100 mA deflector whose pulse width is 4 mm and longitudinal phase occupation is 28.30 is shown in Fig. 14. The convergence of the solution as a function of axial resolution is shown in Fig. 15 for an order of magnitude variation.

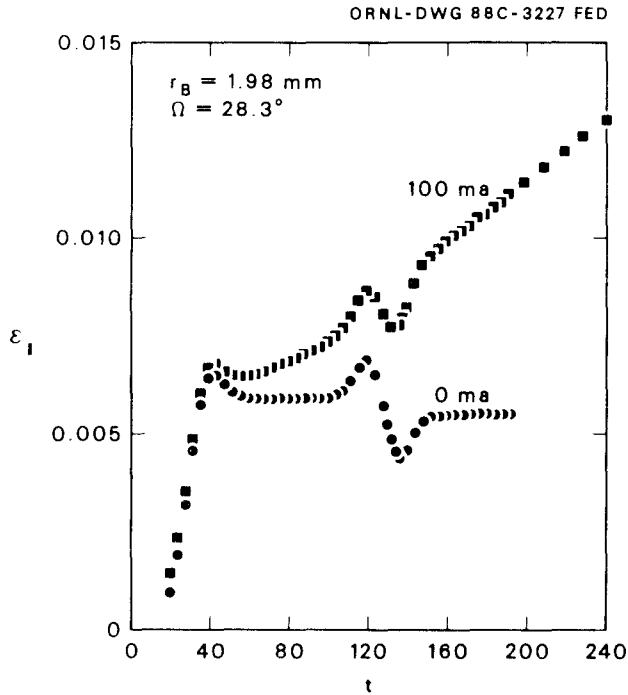


Fig. 14. 100 ma deflector.

4. Three-Dimensional Calculations on RF Deflector

The heart of the deflector in full three-dimension is shown in Fig. 16. Fig. 16(b) is rescaled and the three axes are not the same. The beam is chosen to be a square bunch and is seen drifting approximately in the middle of the device in Fig. 16. Because of the scale of the figure the fact that the rf deflector plates are much longer than the space between them is not evident from the drawing. However, the spacing was indicated previously in the two-dimensional section; for example, Fig. 10 actually reflects the situation. In Fig. 17 is shown again unsealed coordinates of the rf deflector in full three-dimension showing the entrance aperture, the rf parallel plate deflector itself. In this case, in part A of this figure, potential contours on the symmetry axis occur at an instant of time when the pulse happens to be in the middle of the deflector and these fields, at a maximum, are shown. The fringe fields can easily be seen. The contours of the fringe fields are compressed over the contours of the fields in the normal deflection region so as to show the extent of the fringe fields. In part B, the same situation is shown except the 100 mA pulse is being deflected. The pulse happens to be at this time in the middle of the rf deflector plates. On the symmetry axis one can see an indentation. A depression of this equal potential contour

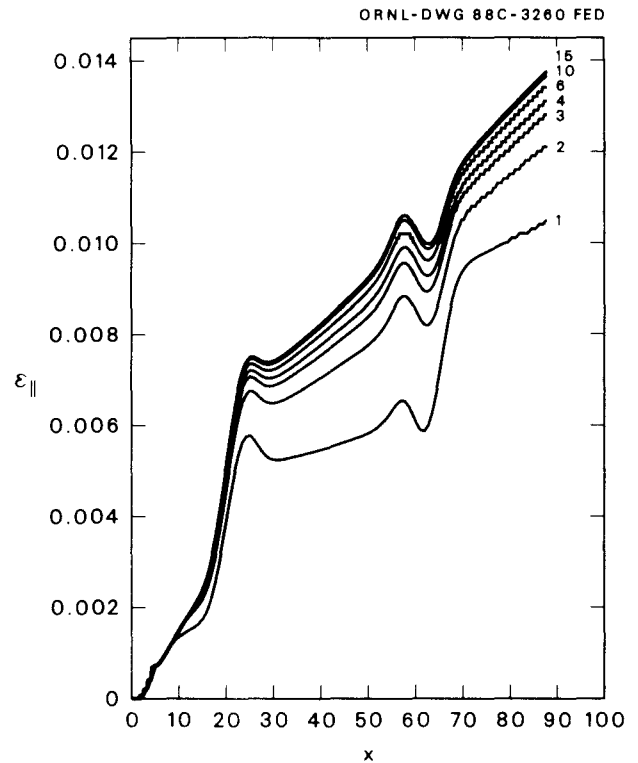


Fig. 15. Convergence as a function of axial resolution.

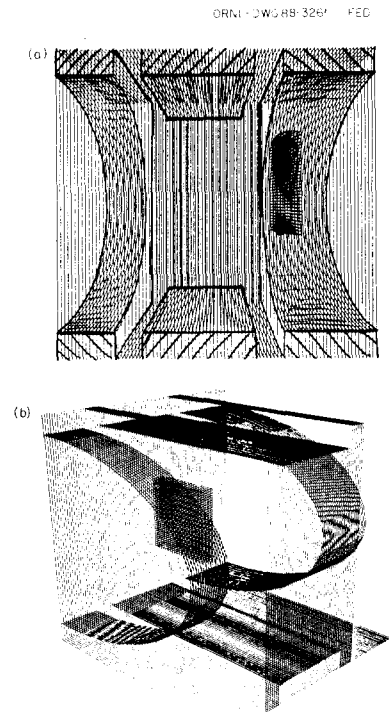


Fig. 16. A deflector in two views.

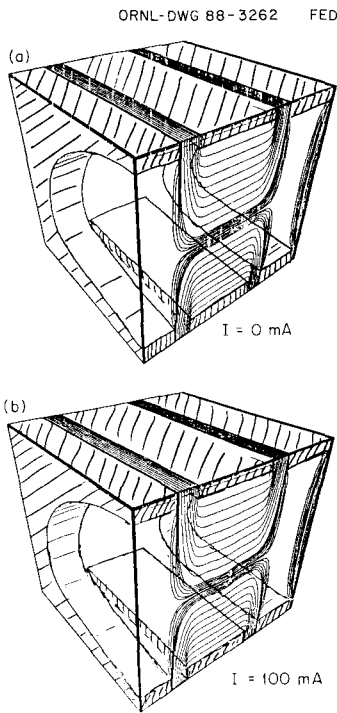


Fig. 17. RF deflector potentials in 3 dimensions.

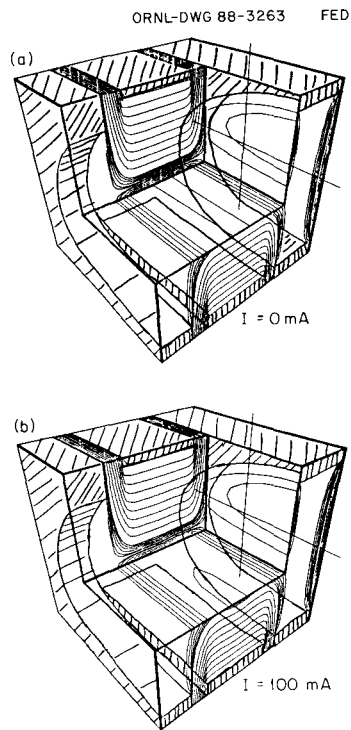


Fig. 18. Rf deflector with fringe fields.

is due to this pulse. This is similar to the findings in the two dimensional situation.

The situation in Fig. 18 is rather similar to Fig. 17, except that here is exhibited explicitly the fringe fields near the aperture. This is the situation shown for both 0 mA and 100 mA current in Fig. 18(a) and 18(b), respectively. The issue is these fringe fields coming from the parallel plate deflector and entering and impinging upon a circular hole at the entrance of the exit aperture. The effect of these fringe fields is a principle result of these three-dimensional calculations.

The parallel emittance growth for these three-dimensional deflectors is shown as a function of time for a particular pulse in Fig. 19. Here we see the characteristic emittance growth at the beginning for either 0 mA or 100 mA current. We see a gradual but slower emittance growth in the region of the rf deflector itself for the case of the 100 mA beam and no growth for the case of the 0 current beam. The various bunches given to the beam at the fringe field upon exiting the deflecting region are shown in both the 100 mA and the 0 mA cases by the twitches thereof, and finally, the post emittance variation is shown. There is no increase of emittance above a certain level for the 0 current beam, which is expected since no nominal space charge forces are present and nothing else would be existing in this region to increase the emittance of the beam. However, as was shown in other cases previously, for the 100 mA beam there is the characteristic nonlinear space charge induced longitudinal emittance growth.

In this case, as in so many cases, the initial distribution of the beam has zero emittance, which corresponds to a shoebox waterbag model. If the emittance was larger to begin with, then the emittance growth fortunately would be presumably less than is shown here. All the emittance growth that we see here is obtained in the funnel itself for a 0 emittance. If the beam, for example, has an initial emittance of 0.005 and a current of 100 mA, then instead of the final emittance being 0.0085 as is shown here at the final time, the final emittance would probably be approximately 0.01, reflecting the quadratic zoning of the emittance growth with the initial emittance of the beam.

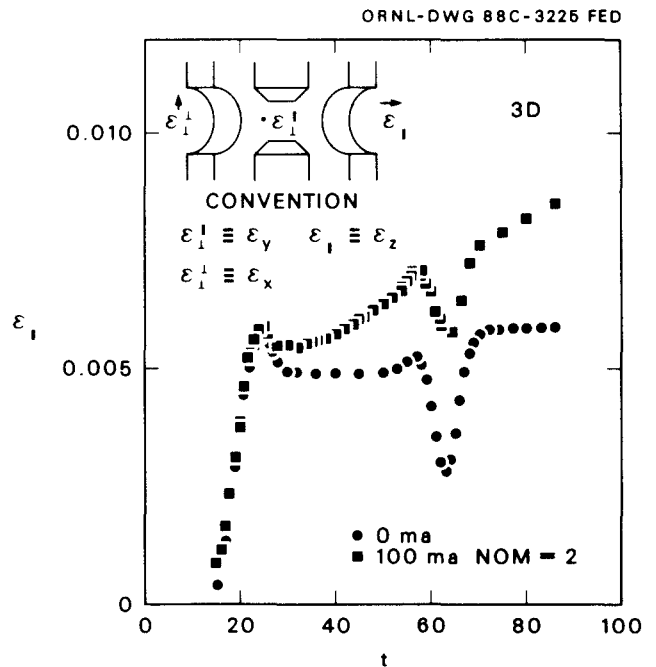


Fig. 19(a). Emittance growth as a function of time.

velocity is characteristic of a rebuncher, which means the beam is compressing. Fig. 24 is after the beam has drifted a significant distance, as shown. This corresponds to point B on Fig. 22. The transverse emittance has increased significantly and the parallel has obviously increased. Enormous aberrations, basically from nonlinear space charge forces between points A and B, can be seen on the longitudinal emittance diagram on the lower right hand side. This is consistent with the curve in point B of Fig. 22. As the beam drifts still further, as indicated in Fig. 25 (corresponding to point C of Fig. 22), it covers an enormous distance. The longitudinal emittance is very high and very different from that presented in Fig. 24. Here the beam is essentially crossing over from a rebunch case to a debunched case. Figure 26, corresponding to point D of Fig. 22, shows the beam transported still further. The beam is now debunching. Space charge forces have caused the beam to expand instead of compress, and the emittance growth is slowing down for the moment, but will increase again as the beam simply expands in a very nonlinear fashion. This kind of growth is a significant concern for intense beams drifting in long, unneutralized transport systems where there is a requirement for very low longitudinal emittance growth.

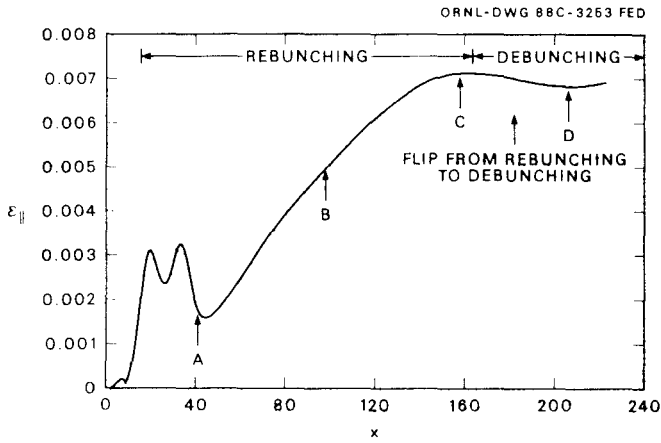


Fig. 22. Hard beam parallel emittance growth for a longer distance.

ORNL-DWG 88-3267 FED

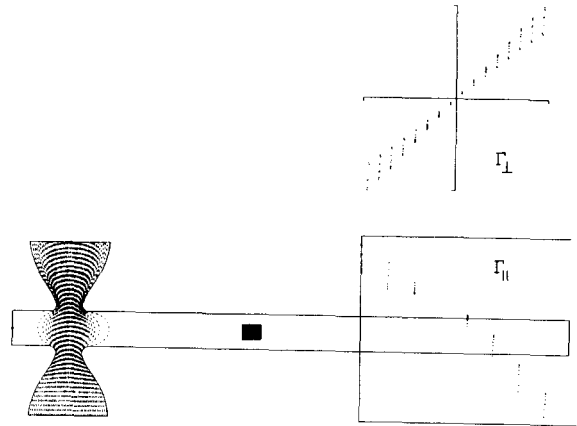


Fig. 24. Same as Figure 23 but at a later date.

ORNL-DWG 88-3268 FED

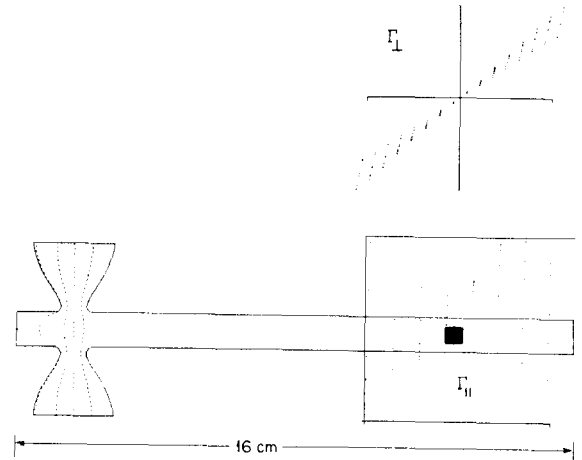


Fig. 25. Yet later.

ORNL-DWG 88-3266 FED

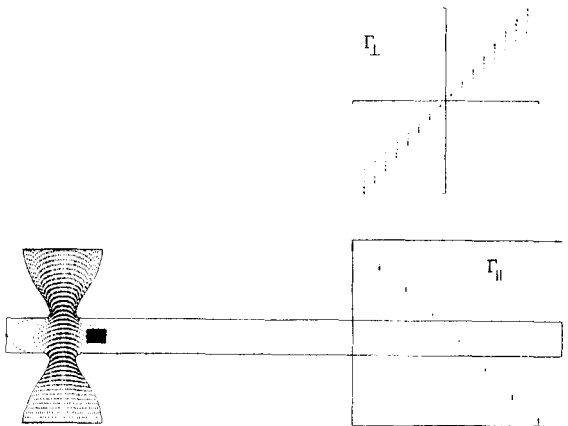


Fig. 23. Simple rebuncher with a beam pulse.

ORNL-DWG 88-3269 FED

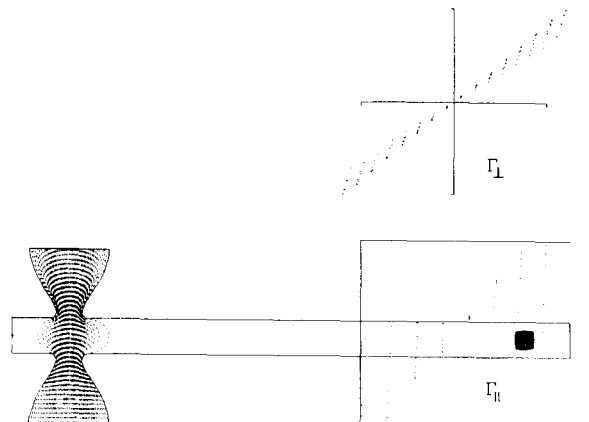


Fig. 26. Yet later: the beam debunching.

6. Conclusions

One embodiment of a funnel will probably contribute to a parallel emittance growth, end to end, of about 0.015 ncm mr, assuming perfect alignment according to calculations performed thus far. The transverse emittance growth is expected to be slightly less, but still on the order of 0.010ncm mr. The value for the parallel emittance may be halved with the deployment of the lens discussed in Section 5.

References

1. K. Bongardt et al., Proc. Symp. Accel. Aspects of Heavy Ion Fusion, GSI-82-8, 224 (1982), also GSI-84-11, 389 (1984); F.W.Guy, AIP Conf. Proc. 139, 207 (1985); F.W. Guy and T.P. Wangler, *ibid*, p. 185.
2. "Ab Initio Calculation of Nonlinear Transient Beam Dynamics for Ion LINAC and Injectors," J.H. Whealton, R.J. Raridon, M.A. Bell, K.E. Rothe, B.D. Murphy, and P.M. Ryan, Workshop on Space Charge Effects in Beam Dynamics, ORNL (1986); "Ion Beam Dynamics in High Intensity RFQ LINAC," J.H. Whealton, R.J. Raridon, M.A. Bell, K.E. Rothe, B.D. Murphy, Twenty-Eighth Annual Meeting of the Division of Plasma Physics of the American Physical Society, Baltimore, Maryland, November 3-7, 1986; 1987 Particle Accelerator Conference, Washington, D.C. March 16-19, 1988, Bull. APS 32, 189 (1987); "3D, Full Implicitly, Ion Time Scale, Self-Consistent Plasma Edge Calculations Near ICRH Antenna/Faraday Shield," J.H. Whealton, P.M. Ryan, and R.J. Raridon, ICRF/Edge Physics Workshop, Boulder, Colorado, March 30, 1988.
3. T.L. Owens, private communications (1987). Some of the PARMILA calculations were done by K. Crandall of AccSys Inc.
4. G. D. Smith, Numerical Solution of Partial Difference Equations: Finite Difference Methods, 2nd ed. (Oxford Univ. Press, Oxford, 1978).
5. J. W. Wooten, J. H. Whealton, D. H. McCollough, R. W. McGaffey, J. E. Akin, and L. J. Dooks, J. Comput. Phys. **43**, 95 (1981); K. Ota, N. Inone, H. Hikei, J. Marikawoo, S. Ishida, and T. Uchida, J. Appl. Phys. **23**, 1241 (1984); J. W. Wooten, J. H. Whealton, and D. H. McCollough, J. Appl. Phys. **52**, 6418 (1981).
6. J. H. Whealton, R. W. McGaffey, and P. S. Meszaros, J. Comput. Phys. **63**, 20 (1986).
7. J. H. Whealton, J. Comput. Phys. **40**, 491 (1981); J. H. Whealton, Nucl. Instrum. Methods **189**, 55 (1981); J. H. Whealton, IEEE Trans. Nucl. Sci. **NS28**, 1358 (1981).
8. J. H. Whealton, E. J. Jaeger, and J. C. Whitson, J. Comput. Phys. **27**, 32 (1978).
9. J. C. Whitson, J. Smith, and J. H. Whealton, J. Comput. Phys. **28**, 408 (1978); J. H. Whealton and J. C. Whitson, Part. Accel. **10**, 235 (1980).
10. E. F. Jaeger and J. C. Whitson, ORNL/TM-4990, 1975.
11. J. M. Ortega and W. D. Rheinboldt, Iterative Solution of Nonlinear Equations in Several Variables (Academic Press, N.Y., 1970).